

**PARALLEL IMPLEMENTATION OF A THREE-DIMENSIONAL
NONLINEAR WAVE MODEL FOR RANDOM DIRECTIONAL SEAS**

by

Nuttita Pophet

A thesis submitted to the Faculty of the University of Delaware in partial fulfillment of the requirements for the degree of Master of Science in Ocean Engineering

Fall 2012

© 2012 Nuttita Pophet
All Rights Reserved

PARALLEL IMPLEMENTATION OF A THREE-DIMENSIONAL
NONLINEAR WAVE MODEL FOR RANDOM DIRECTIONAL SEAS

by

Nuttita Pophet

Approved: _____

James T. Kirby, Ph.D.

Professor in charge of thesis on behalf of the Advisory Committee

Approved: _____

Harry W. Shenton, Ph.D.

Chair of the Department of Civil and Environmental Engineering

Approved: _____

Babatunde A. Ogunnaike, Ph.D.

Interim Dean of the College of Engineering

Approved: _____

Charles G. Riordan, Ph.D.

Vice Provost for Graduate and Professional Education

ACKNOWLEDGMENTS

I would like to thank my advisor, Dr. James T. Kirby, for his support during the time I spent at University of Delaware and giving me the opportunity. It was an excellent opportunity for me to work with him.

I also thank our colleagues in the College of Earth, Ocean and Environment, especially to Dr. Entin Karjadi, Dr. Joseph Senne, Dr. Mohsen Badiey and Dr. Aijun Song for technical discussions about field observation data used for analysis in this thesis. I would also like to thank Dr. Philippe Guyenne for assisting me with the wave model.

I will always gratefully remember my former advisors, Dr. Jack Asavanant and Dr. Mansour Ioualalen for introducing me the field of ocean engineering. Without their support and encouragement I would have never come to this point.

Most of all I would like to thank my beloved parents for their endless support that becomes an invaluable source of strength throughout all these years.

TABLE OF CONTENTS

LIST OF FIGURES	vi
ABSTRACT	viii
Chapter	
1 INTRODUCTION	1
2 WAVE MODEL	5
2.1 Governing Equation	5
2.2 Numerical Method	8
2.2.1 Spatial Discretization	8
2.2.2 Time Integration	9
2.2.3 Error Controlling	10
2.3 Energy Dissipation	11
2.4 Parallel Implementation	12
2.4.1 Parallel Pseudo Algorithm	12
2.4.2 Data Distribution	13
2.4.3 Using the FFTW-MPI Libraries	14
3 PARALLEL MODEL TESTING	15
3.1 Accuracy	15
3.1.1 Solitary Wave	15
3.1.2 Energy Focusing Wave Group	16
3.2 Performance	18

4	DETECTION OF BREAKING EVENTS IN MODELED SEA . .	22
4.1	Wave Breaking Criterion Parameter	22
4.2	Approximation of Vertical Acceleration	22
5	NUMERICAL SIMULATIONS	24
5.1	Testing 1D Wave Breaking	24
5.1.1	Laboratory Experiments	24
5.1.2	Initial Condition and Numerical Simulation Setup	25
5.1.3	Results	27
5.2	Simulation of Sea State	30
5.2.1	Field Observation Data	30
5.2.2	Construction of Initial Wave Field in 3D	31
5.2.3	Numerical Simulation Setup	34
5.2.4	Results	36
6	CONCLUSION	42
	BIBLIOGRAPHY	44

LIST OF FIGURES

2.1	Data distribution for N processes in the FFTW-MPI solver.	13
3.1	Evolution of a solitary wave.	16
3.2	Surface elevation of the wave measured at the first wave station. . .	17
3.3	Sketch of the numerical wave tank. The domain from 20 to 35 m corresponds to the experimental wave tank. The blue dots indicate locations of wave probes.	18
3.4	Surface elevation of the wave in the numerical wave tank at time (a) $t=0s$, (b) $t=10s$ and (c) $t=20s$. The red dots indicate locations of wave probes.	19
3.5	Comparison of the predicted (red) and measured (blue) long time integration of the surface variance.	20
3.6	Evolution of predicted surface displacement.	20
3.7	Speedup and time spent for each time step of the parallel model for the grid size 4096×4096	21
5.1	Surface elevation of the breaking wave groups (a) BG1 and (b) BG2 measured at the first wave station in the laboratory experiments. . .	26
5.2	Surface elevation of the breaking wave group BG1 in the numerical wave tank at time (a) $t=0s$, (b) $t=10s$ and (c) $t=20s$. The red dots indicate locations of wave probes.	28
5.3	Surface elevation of the breaking wave group BG2 in the numerical wave tank at time (a) $t=0s$, (b) $t=10s$ and (c) $t=20s$. The red dots indicate locations of wave probes.	29
5.4	Comparison of the predicted (red) and measured (blue) long time integration of the surface variance of case BG1 and BG2.	30

5.5	Surface power spectral density and direction.	31
5.6	Initial surface elevation.	35
5.7	(a) Map of breaking regions at time 40 s. The red patches indicate regions where the vertical acceleration is less than the threshold of -0.4. (b) Predicted surface elevation at time 40 s. The black circles indicate locations where the model detected wave breaking.	37
5.8	(a) Map of breaking regions at time 400 s. The red patches indicate regions where the vertical acceleration is less than the threshold of -0.4. (b) Predicted surface elevation at time 400 s. The black circles indicate locations where the model detected wave breaking.	38
5.9	(a) Map of breaking regions at time 455 s. The red patches indicate regions where the vertical acceleration is less than the threshold of -0.4. (b) Predicted surface elevation at time 455 s. The black circles indicate locations where the model detected wave breaking.	39
5.10	Percent of breaking point of cases with the strength of the damping constant (a) $\sigma = 0.3$, (b) $\sigma = 1.0$ and (c) $\sigma = 2.0$	40
5.11	Energy density and significant wave height (H_{m0}) as a function of time for cases with the strength of the damping constant $\sigma=0.3, 1.0$ and 2.0	41

ABSTRACT

In this thesis, the three-dimensional nonlinear wave model has been parallelized and extended to include wave breaking and energy dissipation. The model has been examined with simulations of solitary wave and energy focusing nonbreaking wave group in laboratory experiment for accuracy and performance test. The vertical acceleration has been used as a criterion to detect the likely occurrence of wave breaking in numerical simulations. Adding pressure against the wave field is the technique used to dissipate energy.

The model has been applied to simulate energy focusing breaking wave groups from laboratory experiments and ocean sea surfaces generated from real spectrum measured in the Kauai Acoustic Communications MURI experiment (KAM11). The predicted and measured total wave energy has been studied for the numerical simulations of laboratory experiments. For the field observation, ocean sea surface and breaking region have been presented. Percent of breaking points in a numerical domain and energy dissipation have been computed.

Chapter 1

INTRODUCTION

Ocean wave field evolution involves many complicated physical processes, including wind input via air-sea interactions, nonlinear energy transfer through wave-wave interactions and energy dissipation due to wave breaking. Due to these dynamic processes, accurate prediction of the ocean wave field is a very challenging task. In recent years, considerable progress has been made toward prediction of ocean wave field using phase-resolving nonlinear wave models. Various numerical methods which can be used to trace the temporal evolution of wave motion have been proposed. Among them, there are two methods widely accepted in literatures for the phase-resolving nonlinear wave models: a high-order spectral method (HOS) developed by Dommermuth and Yue (1987) and a method using Dirichlet-Neumann operator introduced and expanded by Craig and Sulem (1993). Both models are based on Zakharov's equations (Zakharov, 1968).

By extending the Zakharov/mode-coupling idea, Dommermuth and Yue (1987) developed a direct numerical approach which is a combination of canonical evolution equations and mode coupling idea. The model was generalized to include nonlinear interaction up to an arbitrary order M in wave steepness provided that the Taylor series expansion of the velocity potential on the free surface about the mean water level remains valid. In the study, they indicated that $M = O(10)$ is adequate for waves up to approximately 80% of Stokes limiting steepness ($ka < 0.35$), beyond which convergence is poorer and eventually fails. The efficiency and accuracy of the method is demonstrated by comparisons to fully nonlinear semi-Lagrangian computations, calculations of long-time evolution of wavetrains using the modified (fourth-order) Zakharov equations, and experimental measurements of a travelling wave packet.

Zakharov's formulation has been reworked numerous times, including by Craig and Sulem (1993), who posed the Hamiltonian for the water waves problem in terms of the Dirichlet-Neumann operator (DNO) in the two-dimensional setting. Craig and Sulem described the Taylor expansion of the Dirichlet-Neumann operator in homogeneous powers of the surface elevation η . Each term in this Taylor series can be obtained from a recursion formula and can be efficiently computed by a pseudospectral method using the fast Fourier transform. In the study, the method was illustrated by computing the long time evolution of modulated wave packets and of approximations to the Stokes steady wave train. By imposing a surface pressure they observed surface steepening in large amplitude evolution, and wake and bow wave development for flows with a close to critical Froude number and gave an example of nonlinear evolution of the distribution of energy among normal modes. Later, Schanz (1997) performed time-dependent simulations using a three-dimensional extension of Craig and Sulem's model. Nicholls (1998) applied numerical continuation methods to traveling wave solutions of Craig and Sulem's model to find hexagonal solutions of a water wave problem. Xu and Guyenne (2009) developed and implemented a symplectic, implicit, fourth-order Runge-Kutta scheme for the time integration of the Hamiltonian equations, performed extensive numerical tests on the convergence of the DNO and on the accuracy of the time integration method, including an examination of the effects of de-aliasing and filtering, and applied the model to study a number of three-dimensional, nonlinear wave solutions ranging from crescent waves in deep water to hexagonal waves in shallow water.

In a numerical simulation of ocean wave fields, wave breaking effects have to be included in the model in order to provide a reliable prediction. Due to inherent limitations in the mathematical models mentioned above, it cannot predict an overturning surface and an occurrence of spray induced by wave breaking. The presence of wave breaking may cause the computations to terminate abruptly. Therefore, wave breaking effects have to be dealt with for the calculations to proceed. In this aspect, a twofold approach is necessary: detecting the likely occurrence of wave breaking and then absorbing energy locally from waves that are about to break.

Many criteria have been proposed for the detection of wave breaking events based on field observations, laboratory experiments and numerical studies. Wu and Nepf (2002) segregated three classes of wave breaking criteria: the geometry, kinematics, and dynamics of waves. The geometric criteria are based on local wave shape and global wave steepness. The kinematic criteria are based on particle and phase velocities. The dynamic criteria are based on acceleration at the crest, momentum and energy growth rate, and higher harmonic energy evolution. However, wave breaking criteria based on geometric and kinematic properties are not easily applicable to oceanic observations, mainly due to uncertainties in identifying individual waves and unknown threshold values. Most accessible is the dynamic criterion. As pointed out by Snyder and Kennedy (1983) that among possible threshold variables for breaking criteria, vertical acceleration appears an eminently reasonable candidate. Longuet-Higgins (1963) shows that for a Stokes wave of maximum amplitude the particle acceleration near the vertex is $0.5g$ and is directed radially away from the vertex. This result suggests negative vertical acceleration as a threshold variable with a critical level of $0.5g$. Since the Stokes wave is a solution to the full nonlinear equations of motion and because the breaking criterion is presumably universal, we might expect that in a typical wind-generated sea the critical level should also be $0.5g$. However, according to Snyder et al. (1983) and Ochi and Tsai (1983), the negative vertical acceleration that triggers wave breaking is slightly less than this.

A method which can be used to inhibit the development of a breaking wave is to add a damping term to the free surface boundary conditions. For free surface wave problem in potential flows, a damping term is added to the free surface dynamic boundary condition, or to both the dynamic and kinematic boundary conditions. As pointed out by Cao et al. (1993) that this technique is easy to implement and good for a wide range of frequencies. Although a fairly large damping zone is needed and the amount of damping needs to be tuned, the technique has become more popular for simulations of nonlinear waves because of its ability to handle a wide frequency range.

The objective of this work is to develop a forecasting tool for a nonlinear ocean

wave field, which includes:

- develop parallel model and extend to include effects of breaking and wave energy dissipation
- examine accuracy and performance of the model
- apply the model to forecast nonlinear ocean wave field evolution.

In Chapter 2 of this thesis governing equations of the wave model, their numerical method and wave energy dissipation technique will be explained. Methodology for parallelization of the model which includes parallel pseudo algorithm, data distribution and the FFTW-MPI libraries will be presented. In Chapter 3, parallel model testing in terms of accuracy and performance are presented. An idealized case of solitary wave and energy focusing nonbreaking wave group obtained from a laboratory experiment are used for examining an accuracy of the model while an initial Gaussian wave profile is used for checking performance. In Chapter 4, details of wave breaking criterion are discussed. Wave breaking criterion parameter and method used to approximate vertical acceleration are presented. In Chapter 5, numerical simulations of laboratory experiments for energy focusing breaking wave groups and of field observation for ocean random wave are presented.

Chapter 2

WAVE MODEL

In this study, we develop a parallel code of a three-dimensional nonlinear wave model based on the existing code of Xu and Guyenne (2009) and extend the model to include effects of wave breaking and energy dissipation. In this chapter, governing equation is presented along with numerical scheme used to solve the model equation and methods used to control numerical errors. Technique used to dissipate energy locally from waves that are about to break are discussed. Then, we present method used to implement the parallel model. Here, we use a domain decomposition technique for parallelization, MPI for communication between processes and FFTW-MPI (Frigo and Johnson, 2003) for computation of fft.

2.1 Governing Equation

We consider irrotational wave motion of a homogeneous, incompressible and inviscid fluid over a horizontal impermeable bottom. The flow can be described by a velocity potential $\varphi(\mathbf{x}, z, t)$ such that within the fluid φ satisfies the Laplace equation. Here $\mathbf{x} = (x_1, x_2)$ denotes the horizontal plane, z the vertical direction and t time. The fluid velocity is given by $\mathbf{u} = \nabla\varphi$. The velocity potential satisfies the Laplace equation

$$\nabla^2\varphi = 0 \tag{2.1}$$

which is applied throughout the fluid domain bounded below by the bottom at $z = -h$ and above by the free surface defined by $z = \eta(\mathbf{x}, t)$. The boundary conditions are

$$\partial_z \varphi = 0 \quad \text{on } z = -h \quad (2.2)$$

$$\partial_t \eta + \nabla_{\mathbf{x}} \eta \cdot \nabla_{\mathbf{x}} \varphi - \partial_z \varphi = 0 \quad \text{on } z = \eta \quad (2.3)$$

$$\partial_t \varphi + \frac{1}{2} |\nabla \varphi|^2 + g\eta = 0 \quad \text{on } z = \eta \quad (2.4)$$

where $\nabla_{\mathbf{x}} = (\partial_{x_1}, \partial_{x_2})^\top$ and g denotes the acceleration due to gravity. Surface tension effects are neglected here. We can reduce the dimensionality of the classical potential flow formulation (2.1)-(2.4) of the water wave problem by considering surface quantities as unknowns. This can be achieved by introducing the Dirichlet-Neumann operator (DNO) which takes Dirichlet data $\xi(\mathbf{x}, t) = \varphi(\mathbf{x}, \eta(\mathbf{x}, t), t)$ at the free surface, solves the Laplace equation (2.1) for φ , and returns the corresponding Neumann data (i.e. the normal fluid velocity at the free surface). Here the DNO is defined by

$$\begin{aligned} G(\eta)\xi &= (-\nabla_{\mathbf{x}}\eta, 1)^\top \cdot \nabla \varphi|_{z=\eta} \\ &= (-\nabla_{\mathbf{x}}\eta \cdot \nabla \varphi + \nabla \varphi)|_{z=\eta}. \end{aligned} \quad (2.5)$$

Expressing the velocity potential and its derivatives on the free surface in terms of ξ and $G(\eta)\xi$, and knowing that (2.1) and (2.2) are already satisfied through (2.5), then we can rewrite (2.3) and (2.4) as

$$\partial_t \eta = G(\eta)\xi, \quad (2.6)$$

$$\begin{aligned} \partial_t \xi &= -g\eta - \frac{1}{2(1 + |\nabla \eta|^2)} [|\nabla_{\mathbf{x}} \xi|^2 - (G(\eta)\xi)^2 - 2(G(\eta)\xi) \nabla_{\mathbf{x}} \xi \cdot \nabla_{\mathbf{x}} \eta \\ &\quad + |\nabla_{\mathbf{x}} \xi|^2 |\nabla_{\mathbf{x}} \eta|^2 - (\nabla_{\mathbf{x}} \xi \cdot \nabla_{\mathbf{x}} \eta)^2] \end{aligned} \quad (2.7)$$

These are Hamilton's equations in Zakharov's formulation (Zakharov, 1968) of the

water wave problem in terms of the canonically conjugate variables. The total mass and energy of the system,

$$V = \int_{R^2} \eta dx \quad (2.8)$$

and

$$H = \frac{1}{2} \int_{R^2} [\xi G(\eta)\xi + g\eta^2] dx, \quad (2.9)$$

are an invariant of motion in the problem. Mass and energy conservation can be used to check the global accuracy of the numerical model.

Coifman and Meyer (1985) showed that the Dirichlet-Neumann operator is analytic as a function of η if the supremum norm and Lipschitz norm of η are bounded by a constant. Therefore $G(\eta)$ can be written in terms of a convergent Taylor series

$$G(\eta) = \sum_{j=0}^{\infty} G_j(\eta), \quad (2.10)$$

where each term $G_j(\eta)$ is homogeneous of degree j .

Craig and Sulem (1993) showed that explicit expressions for the G_i 's can be obtained using a recursion formula, which was generalized to three dimensions by Nicholls (1998):

For $j = 2r > 0$,

$$\begin{aligned} G_{2r}(\eta) &= \frac{1}{(2r)!} G_0(|D_{\mathbf{x}}|^2)^{r-1} D_{\mathbf{x}} \cdot \eta^{2r} D_{\mathbf{x}} \\ &\quad - \sum_{s=0}^{r-1} \frac{1}{(2(r-s))!} (|D_{\mathbf{x}}|^2)^{r-s} \eta^{2(r-s)} G_{2s}(\eta) \\ &\quad - \sum_{s=0}^{r-1} \frac{1}{(2(r-s)-1)!} G_0(|D_{\mathbf{x}}|^2)^{r-s-1} \eta^{2(r-s)-1} G_{2s+1}(\eta) \end{aligned} \quad (2.11)$$

and, for $j = 2r - 1 > 0$,

$$\begin{aligned}
G_{2r-1}(\eta) &= \frac{1}{(2r-1)!} (|D_{\mathbf{x}}|^2)^{r-1} D_{\mathbf{x}} \cdot \eta^{2r-1} D_{\mathbf{x}} \\
&\quad - \sum_{s=0}^{r-1} \frac{1}{(2(r-s)-1)!} G_0 (|D_{\mathbf{x}}|^2)^{r-s-1} \eta^{2(r-s)-1} G_{2s}(\eta) \\
&\quad - \sum_{s=0}^{r-2} \frac{1}{(2(r-s-1))!} (|D_{\mathbf{x}}|^2)^{r-s-1} \eta^{2(r-s-1)} G_{2s+1}(\eta)
\end{aligned} \tag{2.12}$$

where $D_{\mathbf{x}} = -i\nabla_{\mathbf{x}}$ and $G_0 = G(0) = |D_{\mathbf{x}}| \tanh(h|D_{\mathbf{x}}|)$ represent Fourier multiplier operators, in the infinite-depth case ($h = +\infty$), G_0 reduces to $|D_{\mathbf{x}}|$.

2.2 Numerical Method

2.2.1 Spatial Discretization

We assume periodic boundary conditions in \mathbf{x} and use a pseudospectral method for spatial discretization of the DNO as well as the equations of motion. This is a natural choice for the computation of G since each term in its Taylor series expansion consists of concatenations of Fourier multipliers with powers of η . More specifically, both function η and ξ are expanded in truncated Fourier series

$$\begin{pmatrix} \eta \\ \xi \end{pmatrix} = \sum_{\mathbf{k}} \begin{pmatrix} \hat{\eta}_{\mathbf{k}} \\ \hat{\xi}_{\mathbf{k}} \end{pmatrix} e^{i\mathbf{k}\cdot\mathbf{x}}, \tag{2.13}$$

where $\mathbf{k} = (k_1, k_2)$ denotes the wavenumber. Application of Fourier multipliers are performed in Fourier space, while nonlinear products are calculated in physical space on a grid $N_1 \times N_2$ points, equally spaced in each direction.

In computations, the Taylor series of G is also truncated by only retaining a finite number of terms,

$$G(\eta) \approx G^M(\eta) = \sum_{j=0}^M G_j(\eta) \tag{2.14}$$

where the order of truncation M is chosen according to the physical problem under consideration.

2.2.2 Time Integration

Time integration of system is performed in Fourier space, so the linear terms can be solved exactly by integrating factor technique. To this aim, we first separate the linear and nonlinear parts and define $u = (\eta, \xi)$. The equations of motion can be written in the form

$$\partial_t u = L(u) + N(u) \quad (2.15)$$

where the linear contribution $L(u)$ is defined by

$$L(u) = Au = \begin{pmatrix} 0 & G_0 \\ -g & 0 \end{pmatrix} \begin{pmatrix} \eta \\ \xi \end{pmatrix} \quad (2.16)$$

and the nonlinear contribution $N(u)$ by

$$N(u) = \begin{pmatrix} (G(\eta) - G_0)\xi \\ -\frac{1}{2(1+|\nabla_{\mathbf{x}}\eta|^2)} [|\nabla_{\mathbf{x}}\xi|^2 - (G(\eta)\xi)^2 - 2(G(\eta)\xi)\nabla_{\mathbf{x}}\xi \cdot \nabla_{\mathbf{x}}\eta \\ + |\nabla_{\mathbf{x}}\xi|^2 |\nabla_{\mathbf{x}}\eta|^2 - (\nabla_{\mathbf{x}}\xi \cdot \nabla_{\mathbf{x}}\eta)^2] \end{pmatrix} \quad (2.17)$$

Then taking the Fourier transform and making the change of variables

$$\hat{u}_{\mathbf{k}}(t) = \phi(t)\hat{v}_{\mathbf{k}}(t) \quad (2.18)$$

where

$$\phi(t) = \begin{pmatrix} \cos(t\sqrt{gG_0}) & \sqrt{\frac{G_0}{g}} \sin(t\sqrt{gG_0}) \\ -\sqrt{\frac{g}{G_0}} \sin(t\sqrt{gG_0}) & \cos(t\sqrt{gG_0}) \end{pmatrix} \quad (2.19)$$

is the fundamental matrix of the linear system

$$\partial_t \hat{u}_{\mathbf{k}} = A \hat{u}_{\mathbf{k}} \quad (2.20)$$

and we obtain the following nonlinear system for $\hat{v}_{\mathbf{k}}$

$$\partial_t \hat{v}_{\mathbf{k}} = \phi^{-1} N(\phi \hat{v}_{\mathbf{k}}) = N(\hat{v}_{\mathbf{k}}). \quad (2.21)$$

(2.21) is solved numerically in time using RK4. We note that including nonlinear terms in the computation posts difficulties in solving the model. First, the implementation is much more complicated since we cannot solve the equation directly. The time integration scheme is needed. Second, time needed to compute those terms is quite large. Last, it brings an error inherit with numerical method. It is hard to control error efficiently. However, the real ocean process is nonlinear so it is still needed to include in the study.

2.2.3 Error Controlling

There are two major sources of numerical error in the present model: aliasing and spurious growth of high wavenumber errors. Methods widely used to reduce aliasing error are computing de-aliased products and filtering, while the effects of high wavenumber errors are usually controlled by filtering alone. In order to control aliasing error in our study, we implement de-aliasing using zero-padding technique in evaluating the Dirichlet-Neumann operator (DNO) and other products in the evaluation of the

nonlinear terms. For reducing the growth of high-wavenumber error, we use a low-pass filter of the form

$$\gamma_k = \begin{cases} 1 & \text{if } |\mathbf{k}| \leq \nu |k_{\max}|, \\ 0 & \text{if } |\mathbf{k}| > \nu |k_{\max}|, \end{cases} \quad (2.22)$$

with typically $\nu = 0.9$. This filter is applied to $\hat{\eta}$ and $\hat{\xi}$ in wavenumber space at every time step.

2.3 Energy Dissipation

To dissipate wave energy in our numerical simulation, we employ a variation of the numerical absorbing beach used by Cao et al.(1993) in order to dissipate energy locally. The basic idea consists of exerting an additional, external pressure on the wave in the vicinity of the location where the likelihood of wave breaking has been detected. By causing the wave to work against this external pressure, the energy necessary to prevent the wave from breaking is extracted from the fluid in a local absorbing patch. Mathematically, this consists of the inclusion of an additional term P_{damp} in the dynamic free-surface boundary condition. P_{damp} is non-existent outside the absorbing patch. Within the patch, we prescribe the following form to the damping term:

$$P_{damp} = \sigma |\nabla \xi|^2 \text{sgn}\left(\frac{\partial \xi}{\partial n}\right) \quad (2.23)$$

The $|\nabla \xi|^2$ term determines the magnitude of the damping. σ is a coefficient that may be varied to increase or decrease the amount of damping. In our simulations, we use $\sigma=0.3, 1.0$ and 2.0 . The signum function ensures that the pressure is acting against

the wave. When the damping term is included to the free surface dynamic boundary condition, (2.7) can be written as

$$\partial_t \xi = R + P_{damp} \quad (2.24)$$

where R represents the right hand side of (2.7).

2.4 Parallel Implementation

We develop the parallel code based on the existing model of Xu and Guyenne (2009). The numerical method of the model is described in the previous section. In addition to previous description, issues with parallelization and communication have to be dealt with. Here, we use MPI for communication between processes. To perform FFT in parallel, we use the FFTW-MPI (version 2.1.5) developed by Frigo and Johnson (2003). The FFTW-MPI is a C subroutine library for computing the DFT in one or more dimensions, for both real and complex data, and for arbitrary input size. In our application, we use only real two-dimensional transform.

2.4.1 Parallel Pseudo Algorithm

An implementation of the parallel model can be described with parallel pseudo algorithm as following.

1. MPI is initialized.
2. MPI process 0 reads simulation parameters from an input file and broadcasts these.
3. Local memory allocations at each process are done. Detail of how to distribute data is described below.
4. Main program begins.
 - MPI process 0 reads initial surface elevation and velocity potential and broadcasts these.
 - Time integration loop begins. FFTW-MPI library is used in this step. Detail of how to use the library is described below.

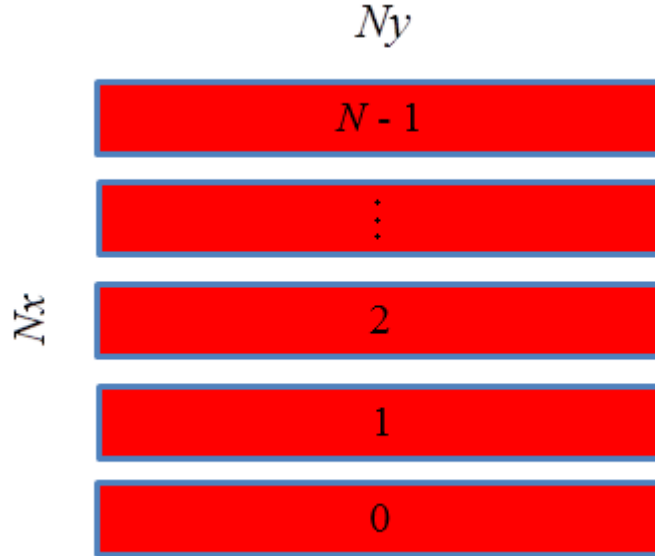


Figure 2.1: Data distribution for N processes in the FFTW-MPI solver.

- Surface elevation and velocity potential are updated and written to a file.
 - If simulation is not over, go to 4.
5. Simulation finished and MPI is terminated.

2.4.2 Data Distribution

For the program to run correctly, the data distribution has to be the way FFTW-MPI defines. The typical decomposition for performing FFT in parallel is slab-wise. With a slab decomposition, the data is partitioned along a single axis. For example, if the global matrix is of size $Nx \times Ny$, the local matrix would be $Nx/N \times Ny$, where N is the number of processes. The global field matrix is divided among the processes as depicted in Fig. 2.1.

The FFTW-MPI provides the following routine to define how much data resides on the current process:

```
fftwnd_mpi_local_sizes(fftwnd_mpi_plan p,
```

```
int *local_nx,  
int *local_x_start,  
int *local_ny_after_transpose,  
int *local_y_start_after_transpose,  
int *total_local_size);
```

We note that `total_local_size` is the number of elements which must be used to allocate local data.

2.4.3 Using the FFTW-MPI Libraries

Usage of the FFTW-MPI routines is similar to that of the uniprocessor FFTW. The following routines are required to perform parallel real two-dimensional transform:

```
alloc_local = fftwnd_mpi_local_sizes(...);  
data = (fftw_real*) malloc(sizeof(fftw_real) * total_local_size);  
solver_forward = rffwnd_mpi_create_plan (... , FFTW_REAL_TO_COMPLEX);  
solver_backward = rffwnd_mpi_create_plan (... , FFTW_COMPLEX_TO_REAL);
```

To execute the solver, we simply state:

```
rffwnd_mpi (solver_forward, data, data);  
rffwnd_mpi (solver_backward, data, data);
```

Chapter 3

PARALLEL MODEL TESTING

A variety of tests have been performed to characterize accuracy and performance of the parallel model. The simulation results presented in this study were performed on the Mills cluster (mills.hpc.udel.edu) which is the University of Delaware high performance computing (HPC) community cluster. It is a distributed memory system consisting of 200 SMP compute nodes with 5,136 cores in total. The Mills cluster uses Scientific Linux6, an open-source Linux distribution of Red Hat Enterprise Linux, as its operating system.

3.1 Accuracy

To examine an accuracy of the parallel model, we performed two different tests with solitary wave and energy focusing wave group in laboratory experiment. For solitary wave we monitor the conserved quantities which are mass and energy for accuracy. For experimental laboratory, we compute the surface variance, which is proportional to the total energy passing a wave station and compare with measured data from the experiment.

3.1.1 Solitary Wave

We consider the propagation of a progressive solitary wave with the same setup as done in Xu and Guyenne (2009). The initial condition is a numerically exact solitary wave generated by Tanaka's method (Tanaka, 1986). The initial wave has amplitude of 0.3 m propagating in shallow water of depth 1 m. The spatial domain considered is of dimension 82 m \times 1.6 m with the number of grid points 256 \times 16. The spatial resolution of the simulation is therefore $\Delta x = 0.32$ m and $\Delta y = 0.1$ m. The nonlinear

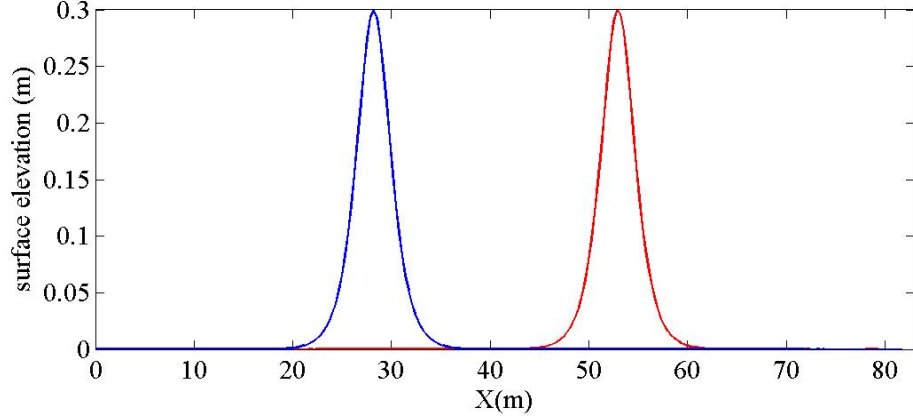


Figure 3.1: Evolution of a solitary wave.

wave field is simulated for an evolution time up to 1000 s with a time step of $\Delta t = 0.01$ s. Nonlinear wave-wave interactions are considered up to the fifth order. The initial wave shape and the wave at the end of the simulation are shown in Fig. 3.1. We can see that the initial wave shape is preserved very well up to $t = 1000$ s. Mass and energy are also conserved very well, with relative errors of $O(10^{-12}\%)$ and $O(10^{-7}\%)$ respectively. There is no filtering required to stabilize the numerical solution. Over the time interval $[0, 1000]$, this wave has propagated a dozen times through the periodic domain $[0, 82\text{m}]$.

3.1.2 Energy Focusing Wave Group

We consider simulations of the energy focusing wave groups which are conducted at Korea Advanced Institute of Science and Technology (KAIST) in a two-dimensional wave tank. As described in Tian et al. (2012), the wave tank is 15 m long, 1.5 m wide, and has a water depth of 0.62 m. Waves are generated with frequencies ranging from 1.0 to 2.4 Hz. The surface elevation is measured using 14 wave probes. The first wave station is located at 1.83 m downstream of the wavemaker. The distance between two adjacent probes ranges from 60 cm to 85 cm. The surface elevation of the wave

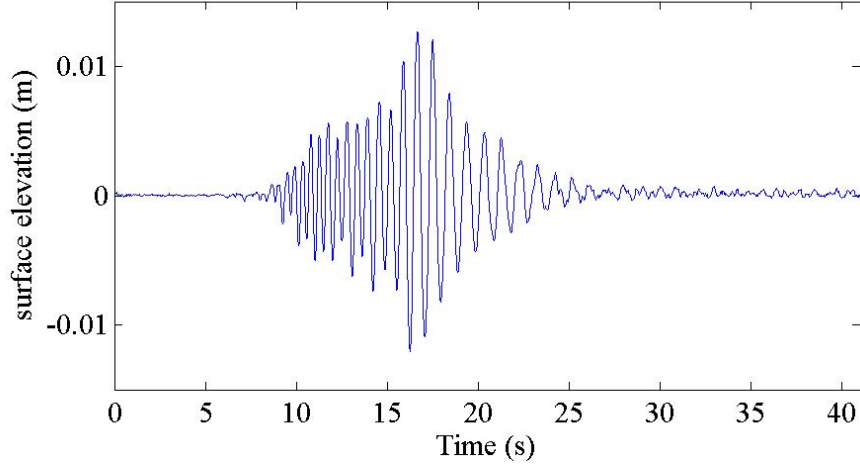


Figure 3.2: Surface elevation of the wave measured at the first wave station.

measured at the first wave station is shown in Fig. 3.2.

To perform numerical simulations, initial conditions for surface elevation and velocity potential are generated using the surface elevation measured at the first wave probe located at 1.83 m of the wave tank. The numerical simulation is performed in a numerical wave tank of 50 m long. The domain from 20 to 35 m corresponds to the physical wave tank. Fig. 3.3 illustrates a sketch of the numerical wave tank. The numerical domain is discretized with 4096 points and a time step of 0.01 s is used in the simulations. The simulation period is 40.96 s. The nonlinear wave-wave interactions are considered up to the fifth order. The surface elevation at time $t = 0, 10$ and 20 s is shown in Fig. 3.4.

Fig.3.5 provides a comparison of the predicted and measured long time integration of the surface variance, which is proportional to the total energy passing a wave station according to linear wave theory. The total potential energy as a function of space is predicted well in the simulation. Fig.3.6 presents the predicted surface elevation at wave stations along the tank.

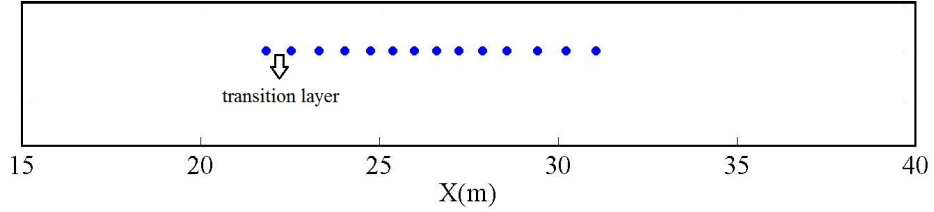


Figure 3.3: Sketch of the numerical wave tank. The domain from 20 to 35 m corresponds to the experimental wave tank. The blue dots indicate locations of wave probes.

3.2 Performance

To investigate performance of the parallel model, we perform numerical simulations of the initial Gaussian wave profile using different number of processors (1, 2, 4, 8, 16, 32, 64 and 128 processors). The nonlinear wave-wave interactions are considered up to the third order with the number of grid points 4096×4096 . The performance results of the parallel model are measured by the parallel speedup. The speedup of n processors is defined as the ratio of the execution time of the parallel model running on a single processor to the execution time of the parallel model running on n processors.

We can see from the plot in Fig. 3.7 that the parallel model have a good scaling with the number of processors increasing until 32. However, the speedup slightly decreases for 64 and 128 processors. We also observe the ratio of time spent in linear to nonlinear model. We found that 91% of simulation time is used for solving nonlinear terms. As we expect in terms of performance of the parallel model, the nonlinear model simulation gives lower speedup. This is because the computation of nonlinear terms involves more FFT computations which require more communication than other parts.

The procedure we use to parallelize the model is to distribute the data over all of the processors and proceed as the serial code does, but with all FFTs done in parallel. The obvious advantage of this procedure is that it adapts well to large problems since it can store more data in memory. However, this style of parallelization tends to not give a good speedup for small problems or even for large problems where large number

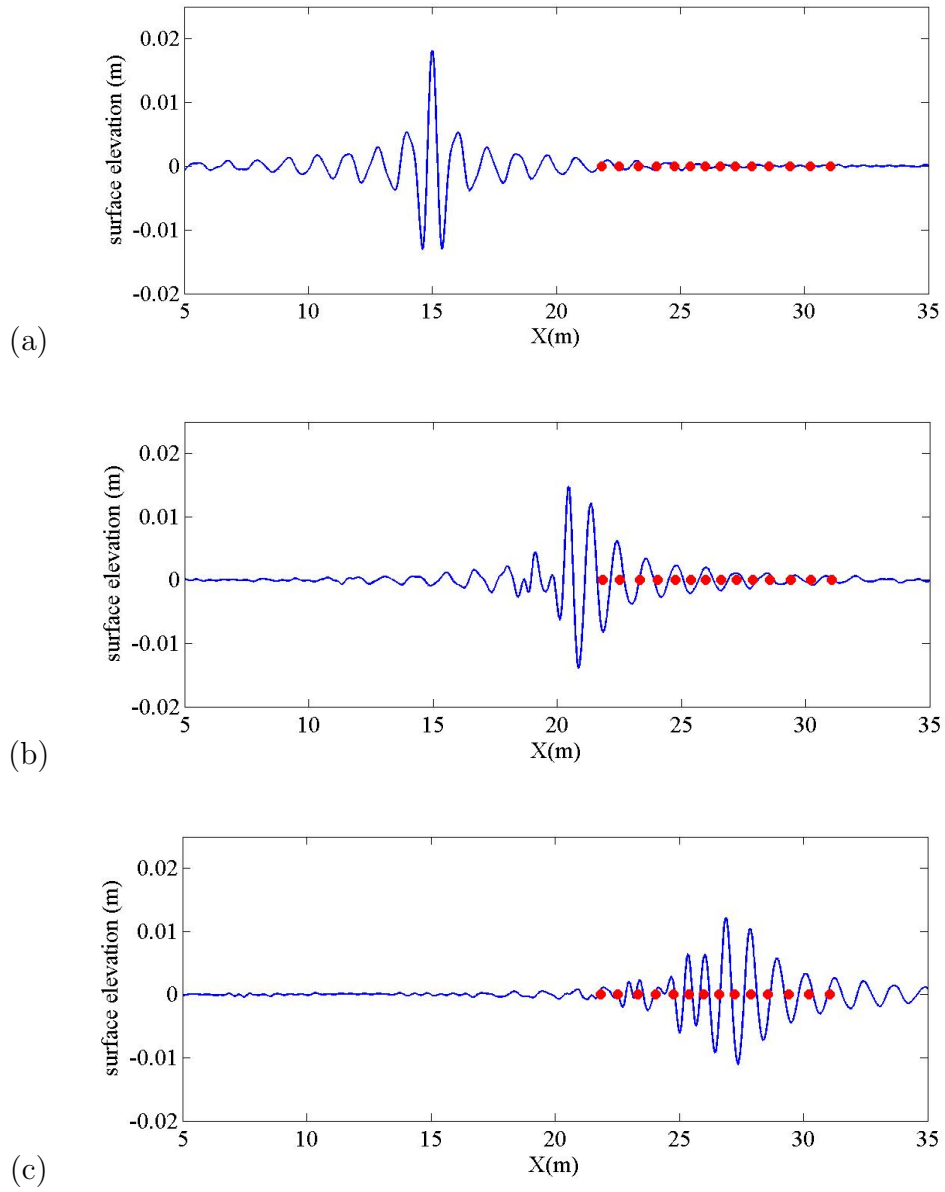


Figure 3.4: Surface elevation of the wave in the numerical wave tank at time (a) $t=0s$, (b) $t=10s$ and (c) $t=20s$. The red dots indicate locations of wave probes.

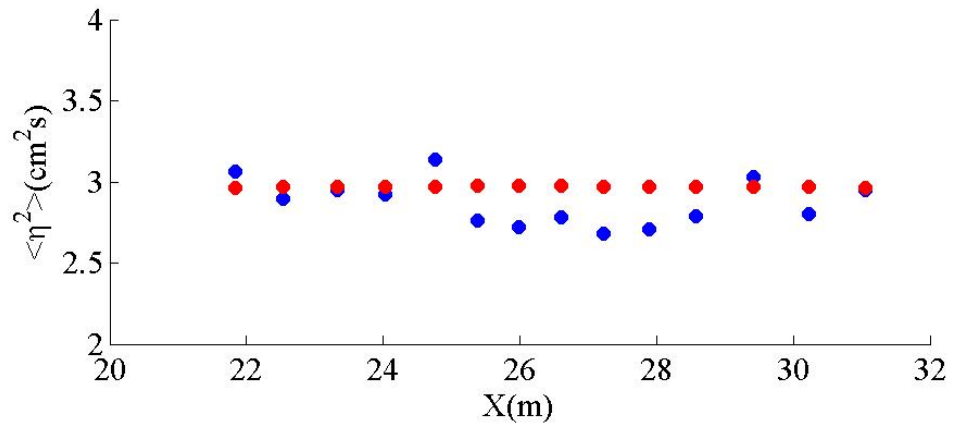


Figure 3.5: Comparison of the predicted (red) and measured (blue) long time integration of the surface variance.

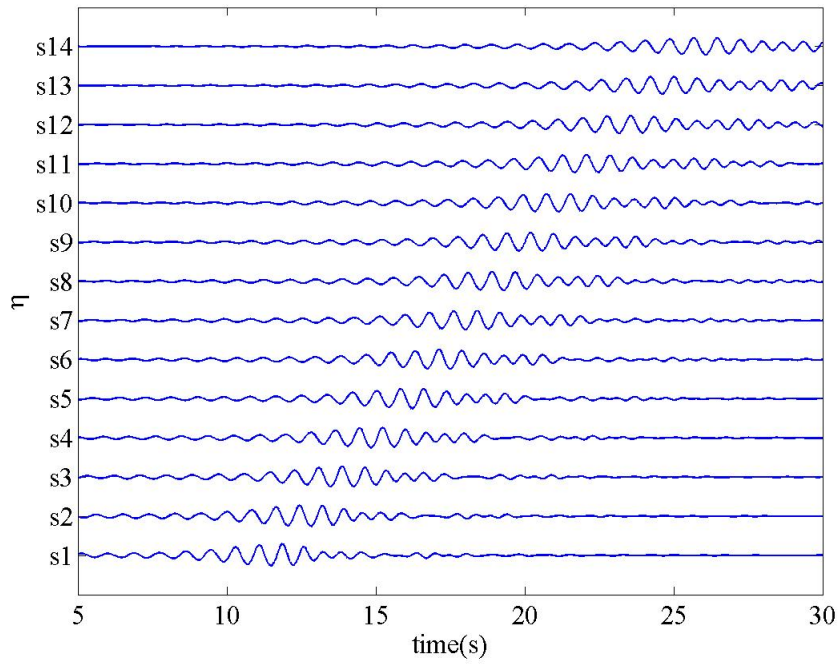


Figure 3.6: Evolution of predicted surface displacement.

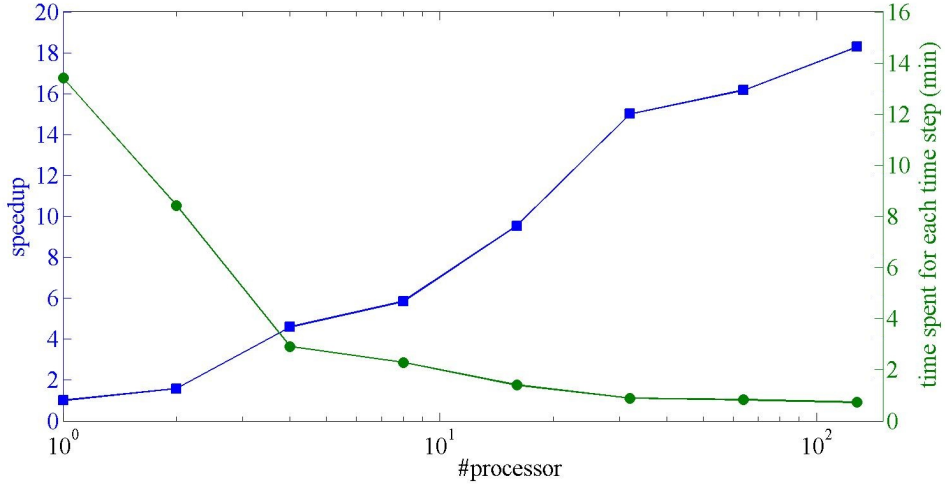


Figure 3.7: Speedup and time spent for each time step of the parallel model for the grid size 4096×4096 .

of processors is used which brings the ratio of communication time to computation time high. Using hybrid method may help improve the speedup. The second level of parallelization could be to parallelize the evaluation of the Dirichlet-Neumann operator as suggested by Nicholls (1998).

We note that our speedup test still have aliasing errors in the results. When we test the speedup we turn off the de-aliasing part since that part will need a lot of global communication. In terms of speed it will be not good to include it. This part will need to be improved in the future to efficiently scale with the number of processors. What may help to improve this is FFTs-alias-free version developed by Roberts (2012). It is a parallel block-based FFTs with C++ based on an openMPI implementation of a block decomposition based parallel FFT code, including option for including implicitly de-aliased convolutions. This will reduce communication costs for both full-data FFTs, and remove all aliasing from communications for zero-padded data. It requires only 12% the bandwidth of conventional techniques.

Chapter 4

DETECTION OF BREAKING EVENTS IN MODELED SEA

As mentioned in Chapter 1, there are several breaking criteria used to detect wave breaking events. However, for random ocean waves, some criteria are not practical to apply. Here, we use the vertical acceleration criterion. In this chapter, the wave breaking criterion and method used to approximate vertical acceleration are discussed.

4.1 Wave Breaking Criterion Parameter

As pointed out by Snyder and Kennedy (1983), among possible threshold variables for breaking criteria summarized in their paper, vertical acceleration appears to be an eminently reasonable candidate. The idea is that if the local surface acceleration at a wave crest reaches some fraction of the gravitational acceleration g , the wave would then break. In order to detect breaking waves in our numerical simulations, we apply the vertical acceleration criterion and scale it with g . In other words, waves will break when the downward acceleration at the crest of the wave is less than $-\alpha g$, i.e.

$$a_z = -\alpha g \tag{4.1}$$

in which α is a constant. According to Snyder et al. (1983), α varies from 0.4 to 0.52, while laboratory experiments of Ochi and Tsai (1983) provide the value $\alpha \approx 0.4$.

4.2 Approximation of Vertical Acceleration

It should be pointed out there are two different vertical accelerations depending on the measurement procedure, i.e. the apparent acceleration measured by a fixed vertical probe, and the real acceleration of the fluid particles, as measured by a small,

free-floating buoy following the sea surface (Longuet-Higgins, 1985). In linearized theory these two accelerations are equal. We apply the apparent acceleration as a criterion for wave breaking in our study.

In two dimensions, consider steady, uniform gravity waves traveling with phase-speed c in the positive x -direction. If the surface elevation is $z = \eta(x, t)$ then the apparent vertical acceleration, as seen by a fixed vertical wave gauge, is η_{tt} . Transforming to a frame of reference moving with speed c , the fluid motion becomes steady. In the new coordinates, η_t is replaced by $-c\eta_x$. The apparent vertical velocity is thus proportional to the surface slope η_x . The apparent acceleration $a^{(E)}$ (Longuet-Higgins, 1985) is given by

$$a^{(E)} = c^2\eta_{xx}. \quad (4.2)$$

In our study, we use the phase speed $c_p = \omega_p/k_p$ at the peak of the spectrum where the peak frequency $\omega_p = 2\pi f_p$ and from the linear dispersion relation the peak wavenumber $k_p = 4\pi^2 f_p^2/g$. For three dimensional application, η_{xx} in (4.2) is simply replaced by $\nabla_x^2\eta$.

We note that practical criteria of wave breaking cannot be based on the instantaneous surface for irregular waves since it will produce a very noisy signal (Massel, 2007). Therefore, it is useful to filter out some random components by suitable smoothing technique. In our case, we use a bandpass filtering with upper and lower cutoffs at $0.5f_p$ and $2.0f_p$, where f_p is the peak spectral frequency.

Chapter 5

NUMERICAL SIMULATIONS

Two cases are studied in this Chapter: laboratory experiments and field observation. The laboratory experiments for energy focusing wave groups were conducted at Korea Advanced Institute of Science and Technology (KAIST) (Tian et al., 2012). The field observation of ocean random wave was conducted in the 2011 Kauai Acoustic Communications MURI experiment (KAM11). Data from both cases is used to generate an initial condition for a numerical simulation. The parallelized model is used to propagate waves in a numerical domain. Detection of wave breaking events in the simulations is done using vertical acceleration criterion and wave energy is dissipated locally. For the laboratory experiment case, we compare wave energy obtained from the simulations with the one obtained from the experiments. For the field observation of ocean random waves, we observe percentage of breaking point in the numerical domains and energy dissipation varied with different parameters.

5.1 Testing 1D Wave Breaking

In this Section, details of laboratory experiment setup are presented. The process of generating initial condition for numerical simulations from experimental data is also described. Then, we describe numerical simulation setup and present results.

5.1.1 Laboratory Experiments

As described in Tian et al. (2012), the wave tank used in the experiments is 15 m long, 1.5 m wide, and has a water depth of 0.62 m. Breaking wave groups due to

wave energy focusing are generated. The surface elevation, η , is defined as

$$\eta(x, t) = \sum_{n=1}^N a_n \cos(k_n x - \omega_n t - \phi_n). \quad (5.1)$$

Here, a_n is the amplitude of the n th wave component; k_n is the wavenumber; $\omega_n = 2\pi f_n$ is the angular frequency and f ranges from 1.0 to 2.4 Hz; $N = 128$ is the total number of frequency components; and ϕ_n is the initial phase to be determined. The linear dispersion relation is used to relate ω_n and k_n . Wave steepness, $\epsilon_n = k_n a_n$, for each of the components is the same and can be adjusted. Two breaking wave groups from the experiment are used in our numerical simulations, referred to as BG1 and BG2. Wave steepness, ϵ_n of BG1 and BG2 is 0.0045 and 0.0058, respectively. During the experiments, the surface elevation is recorded using 14 wave probes. The first wave probe is located at 1.83 m downstream of the wavemaker. The distance between two adjacent probes ranges from 60 cm to 85 cm. Fig. 5.1 shows the surface elevation of the breaking wave groups BG1 and BG2 measured at the first wave probe.

5.1.2 Initial Condition and Numerical Simulation Setup

To perform numerical simulations, initial conditions for surface elevation and velocity potential are generated using the recorded temporal surface elevations at the first wave probe located at 1.83 m of the wave tank. Based on linear wave theory, after it is Fourier decomposed into sinusoidal components, the measured surface elevation can be used to predict the surface elevation using

$$\eta(x, t_0) = \sum_{n=1}^N a_n \cos(k_n(x - x_p)) \quad (5.2)$$

and velocity potential using

$$\xi(x, t_0) = \sum_{n=1}^N \frac{g}{\omega_n} a_n \sin(k_n(x - x_p)). \quad (5.3)$$

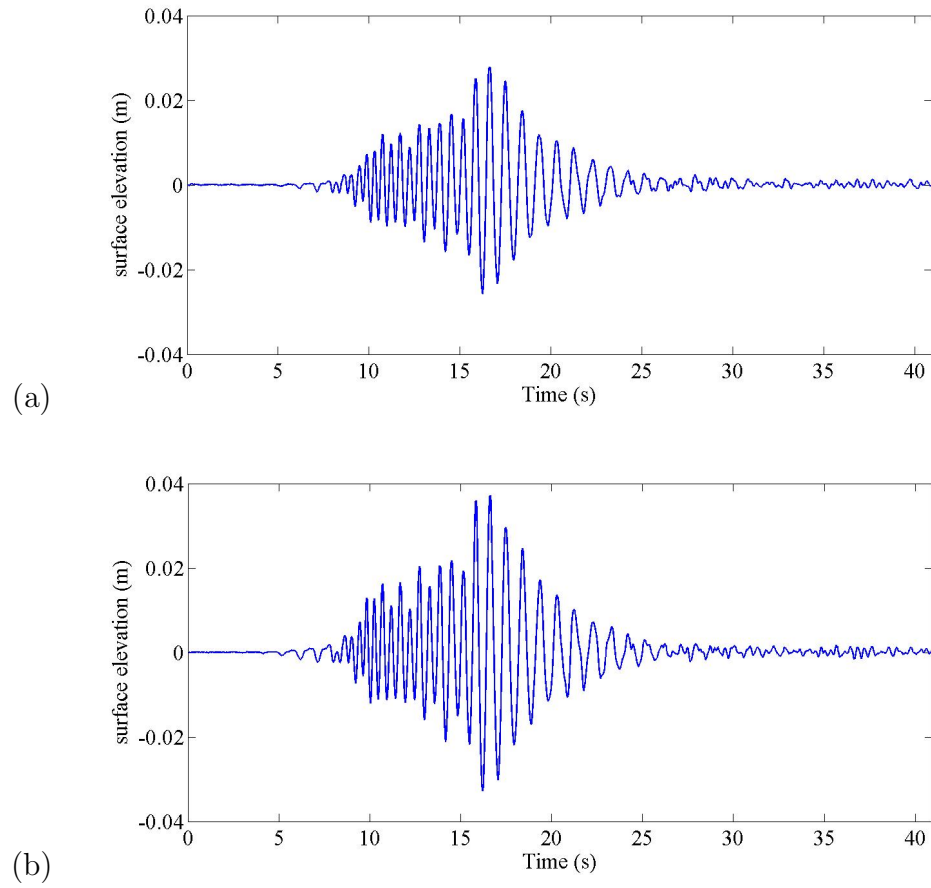


Figure 5.1: Surface elevation of the breaking wave groups (a) BG1 and (b) BG2 measured at the first wave station in the laboratory experiments.

Here, we use $t_0 = 0$ and $x_p = 15$. The simulations are performed in a numerical wave tank of 50 m long. The domain from 20 to 35 m corresponds to the experimental wave tank (see Fig. 3.3 for sketch of the numerical wave tank). The numerical domain is discretized with 4096 points and a time step of 0.01 s is used in the simulations. The simulation period is 40.96 s which is sufficient for the wave groups to completely pass the last wave probe. The nonlinear wave-wave interactions are considered up to the fifth order.

During the simulation, at each time step, the model will detect the likely occurrence of wave breaking based on limiting vertical acceleration criterion. The threshold of $\alpha = -0.4$ is used in the simulations. The vertical acceleration is approximated using curvature of surface displacement at each time. After breaking regions are defined, the model will determine the appropriate amount of local damping. The damping constant $\sigma = 0.3$ is used in the simulations.

To match the surface elevation measured at the first wave gauge, the linear model is solved over the spatial domain from 0 to 21.83 m. In the remainder of the numerical tank, the fifth order model is solved. A transition layer is applied from 21.83 to 22.08 m to avoid any transition irregularity of the surface profile.

5.1.3 Results

Simulations of the breaking wave groups BG1 and BG2 are performed. The surface elevation at time $t = 0, 10$ and 20 s of the wave groups BG1 and BG2 are shown in Fig. 5.2 and Fig. 5.3, respectively.

Fig. 5.4 presents a comparison of the predicted and measured long time integration of the surface variance, which is proportional to the total energy passing a wave station according to linear wave theory. The total potential energy as a function of space for both wave groups is predicted well in the simulations. The results indicate that the breaking model simulates reasonably well the total energy dissipation in the breaking events.

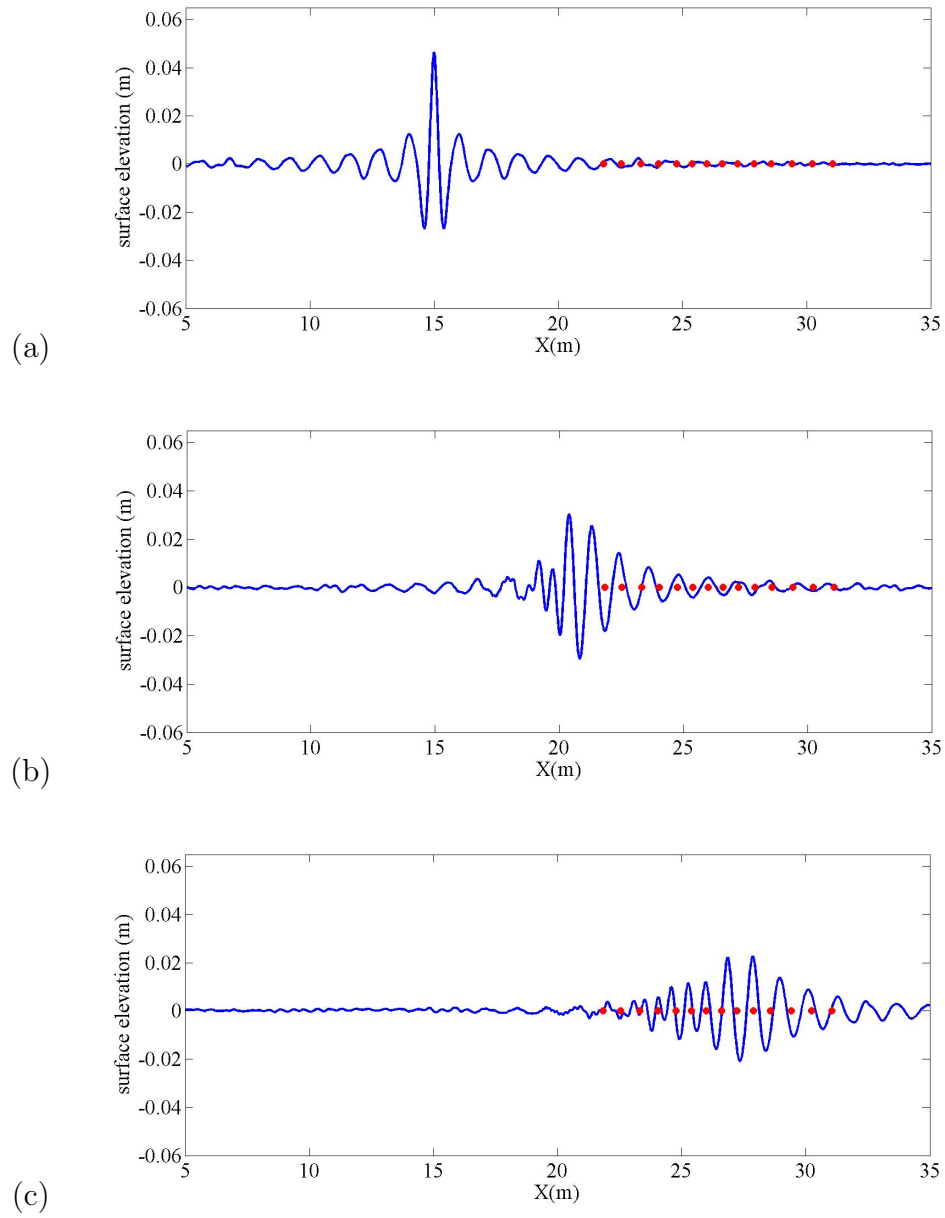


Figure 5.2: Surface elevation of the breaking wave group BG1 in the numerical wave tank at time (a) $t=0s$, (b) $t=10s$ and (c) $t=20s$. The red dots indicate locations of wave probes.

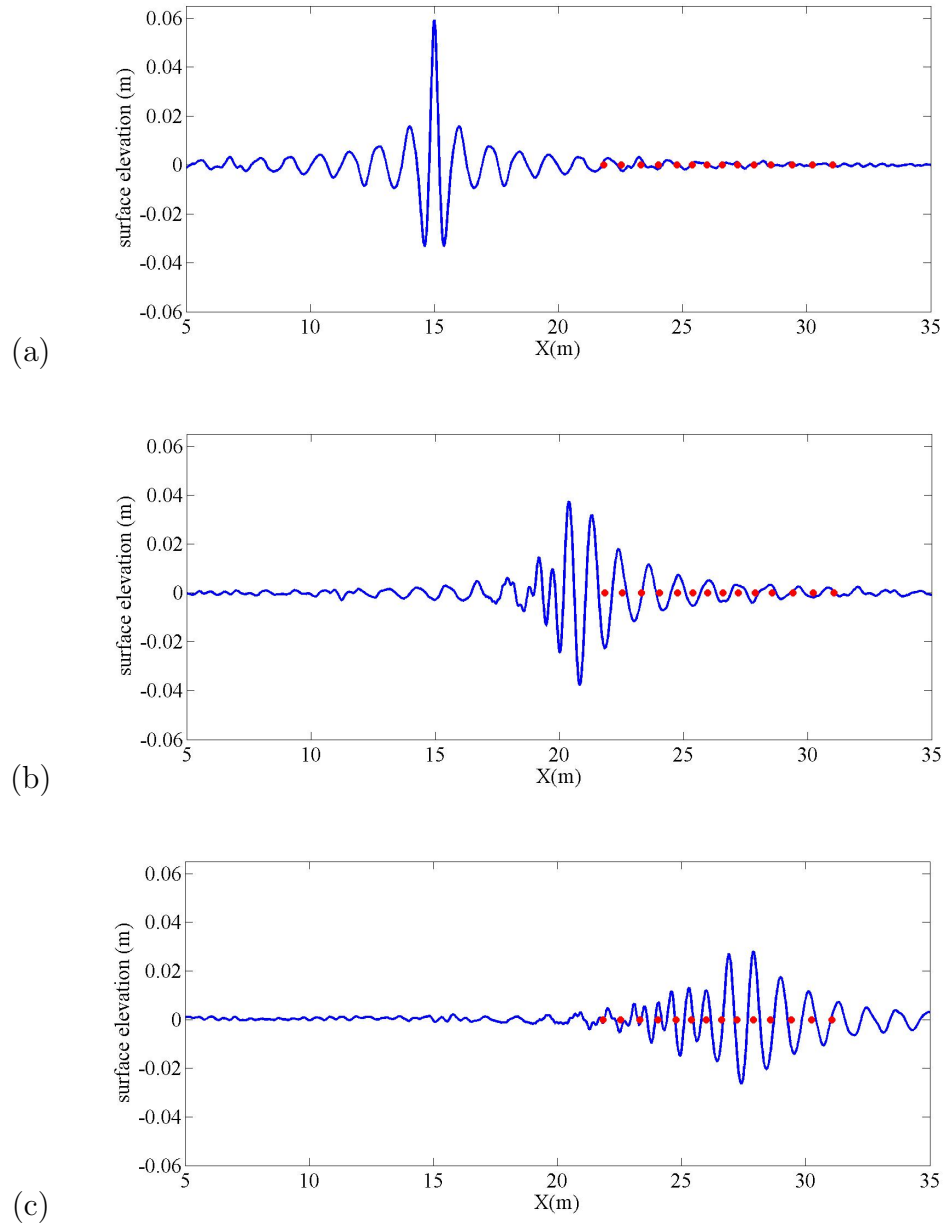


Figure 5.3: Surface elevation of the breaking wave group BG2 in the numerical wave tank at time (a) $t=0s$, (b) $t=10s$ and (c) $t=20s$. The red dots indicate locations of wave probes.

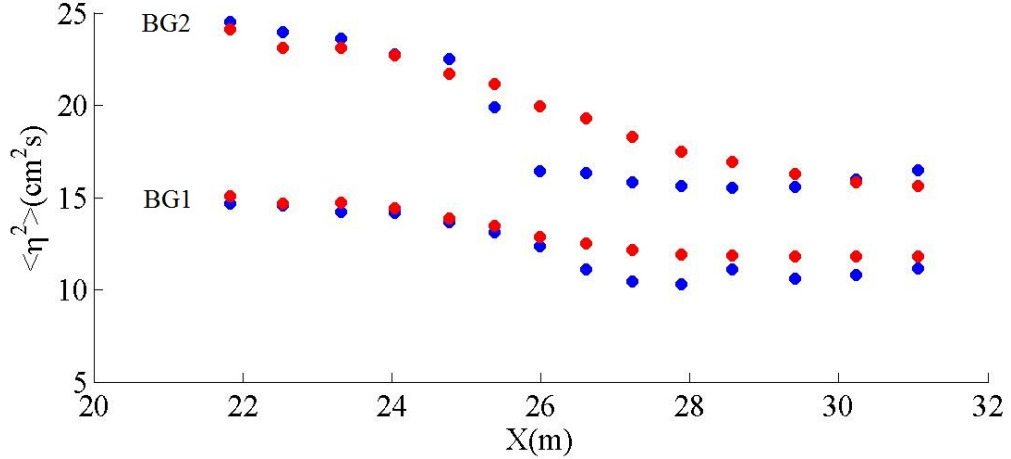


Figure 5.4: Comparison of the predicted (red) and measured (blue) long time integration of the surface variance of case BG1 and BG2.

5.2 Simulation of Sea State

The problem of nonlinear random fields of surface gravity wave is studied in this Section. Details of field observation data are given. The method used to construct initial wave field from constructed from the 2011 Kauai Acoustic Communications MURI experiment (KAM11) is described. Then, the numerical simulation setup and results are presents.

5.2.1 Field Observation Data

A dataset we studied in this Section was collected from the experiment on July 11 at 02:00. This dataset was selected to study because it was the most violent case in the period of the acoustic propagation under water experiment. A wave-rider buoy recorded directional surface displacement throughout KAM11. Fig. 5.5 shows surface power spectral density and direction. The power spectral density from the period of interest shows that the majority of the energy within the surface waves was concentrated in frequency ranges of around 0.1 to 0.3 Hz. From the observed data, the following characteristics are determined. The significant wave height (H_s) is 1.36 m. The peak frequency (f_p) is 0.13 Hz and the zero-upcross period (T_z) is 4.94 s.

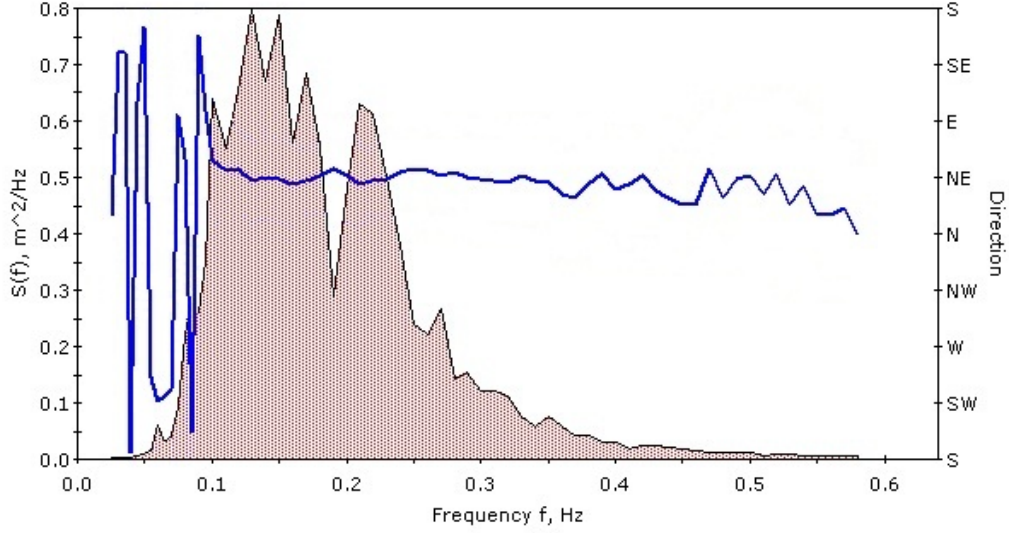


Figure 5.5: Surface power spectral density and direction.

The significant spectral peak steepness, which is an indicator of wave group nonlinearity, is defined as

$$\epsilon_p = \frac{H_s k_p}{2} \quad (5.4)$$

where H_s is the significant wave height and k_p is the peak wavenumber corresponding to the peak frequency f_p by $k_p = (2\pi f_p)^2/g$. In our case, ϵ_p is 0.05.

5.2.2 Construction of Initial Wave Field in 3D

We begin with a power spectral density of the wave field that is frequency-dependent and direction-dependent. From the frequency spectrum $S(\omega)$, we can obtain a wavenumber spectrum $S(k)$ by considering the energy equality under both curves which leads to

$$S(\omega) \frac{d\omega}{dk} = S(k) \quad (5.5)$$

The relationship between ω and is given by dispersion relationship

$$\omega^2 = gk \tanh(kh) \quad (5.6)$$

from which the expression for group velocity can be derived

$$\frac{\partial \omega}{\partial k} = C_g = \frac{1}{2} \left(1 + \frac{2kh}{\sinh(2kh)} \right) \frac{\omega}{k}. \quad (5.7)$$

In 3D, we need to consider directional spreading of waves and work in terms of directional wave spectra. Directional wave spectra $S(k, \theta)$ can be described by

$$S(k, \theta) = S(k)D(\theta) \quad (5.8)$$

where $D(\theta)$ is the directional spreading function. Following Donelan et al. (1985), we use the following form for the directional spreading function

$$D(\theta) = \frac{\beta}{2} \text{sech}^2(\beta(\theta - \bar{\theta})) \quad (5.9)$$

where $\bar{\theta}$ is the mean wave direction and

$$\beta = \begin{cases} 2.61 \left(\frac{\omega}{\omega_p} \right)^{1.3} & ; 0.56 < \frac{\omega}{\omega_p} < 0.95 \\ 2.28 \left(\frac{\omega}{\omega_p} \right)^{-1.3} & ; 0.95 < \frac{\omega}{\omega_p} < 1.6 \\ 1.24 & ; \text{otherwise.} \end{cases} \quad (5.10)$$

We note that in our study the direction at the peak frequency is used instead of the

mean wave direction in (5.9). Next, energy equality is used to transfer from $S(k, \theta)$ to $S(k_x, k_y)$ via division by the Jacobian of the transformation $|J|$ which is given by

$$|J| = \begin{vmatrix} \cos \theta & \sin \theta \\ -k \sin \theta & k \cos \theta \end{vmatrix} = k. \quad (5.11)$$

From $S(k_x, k_y)$ to the two-dimensional amplitude spectrum

$$\frac{1}{2}a_{l,m}^2 = S(l dk_x, m dk_y) dk_x dk_y \quad (5.12)$$

where $l = -\frac{N_x}{2}, -\frac{N_x}{2} + 1, \dots, \frac{N_x}{2} - 1$, $m = -\frac{N_y}{2}, -\frac{N_y}{2} + 1, \dots, \frac{N_y}{2} - 1$, $dk_x = 2\pi/L_x$ and $dk_y = 2\pi/L_y$. N_x is the total number of wave components in x direction, N_y is the total number of wave components in y direction and L_x, L_y are lengths of periodic domain in x and y directions, respectively.

Complex amplitude are computed by using (5.12). A uniformly distributed random number generator with numbers generated in the interval of $[0, 2\pi]$ is used in order to obtain a random representation of the surface by using

$$A_{l,m} = \frac{a_{l,m}}{2} \exp[i\Theta_{l,m}]. \quad (5.13)$$

Similarly for the complex amplitudes used in the construction of surface velocity potential, we have

$$B_{l,m} = -\frac{ig}{\omega_{j,n}} \frac{a_{l,m}}{2} \exp[i\Theta_{l,m}]. \quad (5.14)$$

Then, initial surface elevation can be obtained by

$$\eta_{p,q} = \sum_{l=-N_x/2}^{N_x/2-1} \sum_{m=-N_y/2}^{N_y/2-1} A_{l,m} \exp(ik_l x_p + ik_m y_q) \quad (5.15)$$

and initial surface velocity potential can be obtained by

$$\xi_{p,q} = \sum_{l=-N_x/2}^{N_x/2-1} \sum_{m=-N_y/2}^{N_y/2-1} B_{l,m} \exp(ik_l x_p + ik_m y_q). \quad (5.16)$$

where $p = 0, 1, \dots, N_x - 1$ and $q = 0, 1, \dots, N_y - 1$, $x_p = p dx$, $y_q = q dy$, $dx = L_x/N_x$ and $dy = L_y/N_y$. In order to get real values for η and ξ complex amplitudes A and B have to be complex conjugates. Computation of (5.15) and (5.16) are done by making use of 2D Inverse Fast Fourier Transforms to obtain η and ξ .

5.2.3 Numerical Simulation Setup

After the surface displacement and velocity potential are generated, the wave is propagated in a numerical domain. Here, the spatial domains considered are of dimension $500\text{m} \times 500\text{m}$ with the number of grid points 256×256 . The spatial resolution of the simulation is therefore $\Delta x = \Delta y = 1.95$ m. The nonlinear wave field is simulated for an evolution time up to 1200 seconds or $155T_p$ with a time step of $\Delta t = 0.02$ s or $T_p/385$. The nonlinear wave-wave interactions are considered up to the fifth order. Fig. 5.6 illustrates the initial surface elevation. The color bar represents the scale in meter.

During the simulation, at each time step, the model will detect the likely occurrence of wave breaking based on limiting vertical acceleration criterion. The threshold of $\alpha = -0.4$ is used in the simulations. The vertical acceleration is approximated using curvature of surface displacement at each time. After breaking regions are defined, the model will determine the appropriate amount of local damping. The damping constants of $\sigma = 0.3, 1.0$ and 2.0 are used in the simulations. As mentioned previously in Chapter 4 that smoothing technique is used in detection of wave breaking, here the frequency range $0.06 - 0.26$ Hz is used.

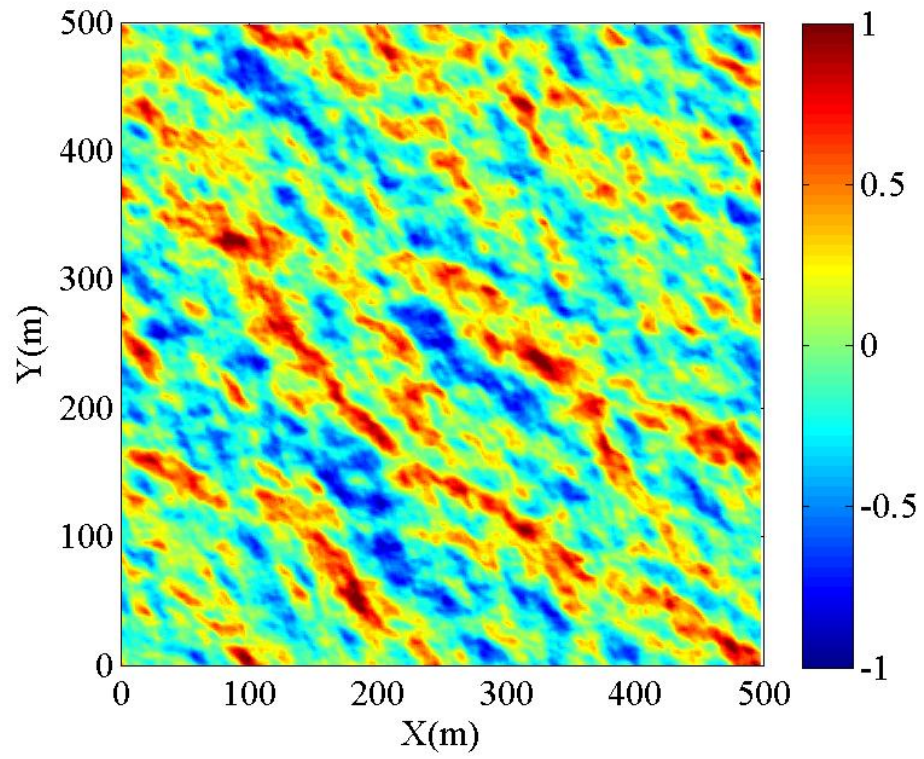


Figure 5.6: Initial surface elevation.

5.2.4 Results

Fig. 5.7 - 5.9 show maps of breaking regions and surface elevations obtained from the numerical simulations at time 40, 400, and 455 s, respectively. These times are selected to present because percent of breaking area during these times is higher than other times. The red patches in Fig. 5.7(a) - 5.9(a) indicate regions in the numerical domains where the vertical acceleration is less than the threshold of -0.4. The black circles in Fig. 5.7(b) - 5.9(b) indicate locations where the model detected wave breaking.

We monitor fraction of breaking region as a function of time. Fig. 5.10 shows percent of breaking point for cases with the strength of the damping constant $\sigma = 0.3$, 1.0 and 2.0, respectively. We can see that percent of breaking point of cases $\sigma = 0.3$ and 1.0 ranges between 0.0 - 1.5 and between 0.0 - 1.0 for case $\sigma = 2.0$. We can also see from Fig. 5.10 that percent of breaking point of case $\sigma = 2.0$ is less than cases $\sigma = 0.3$ and 1.0 and case $\sigma = 1.0$ is less than case $\sigma = 0.3$. This is because the strength of the damping constant, σ , indicates the amount of energy taken from the wave field. The larger σ the more wave energy taken.

During the simulations, the mean wave energy density (E) per unit horizontal area (J/m^2) is computed using linear wave theory, $E = \rho g m_0$ where m_0 is the variance of the surface elevation. Significant wave height (H_0) is computed by $H_{m0} = 4\sqrt{m_0}$. The mean wave energy density and the significant wave height of case $\sigma = 0.3$, 1.0 and 2.0 are shown in Fig. 5.11.

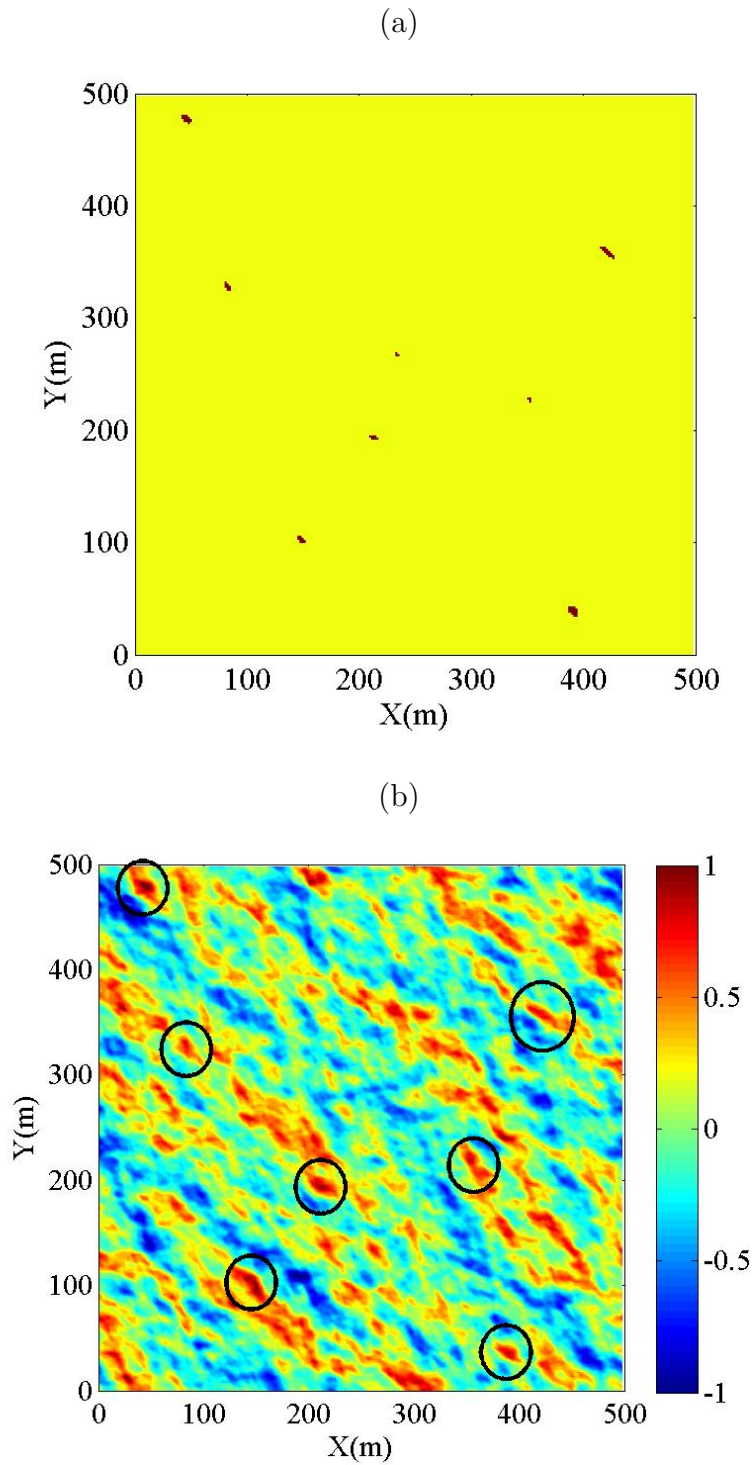


Figure 5.7: (a) Map of breaking regions at time 40 s. The red patches indicate regions where the vertical acceleration is less than the threshold of -0.4 . (b) Predicted surface elevation at time 40 s. The black circles indicate locations where the model detected wave breaking.

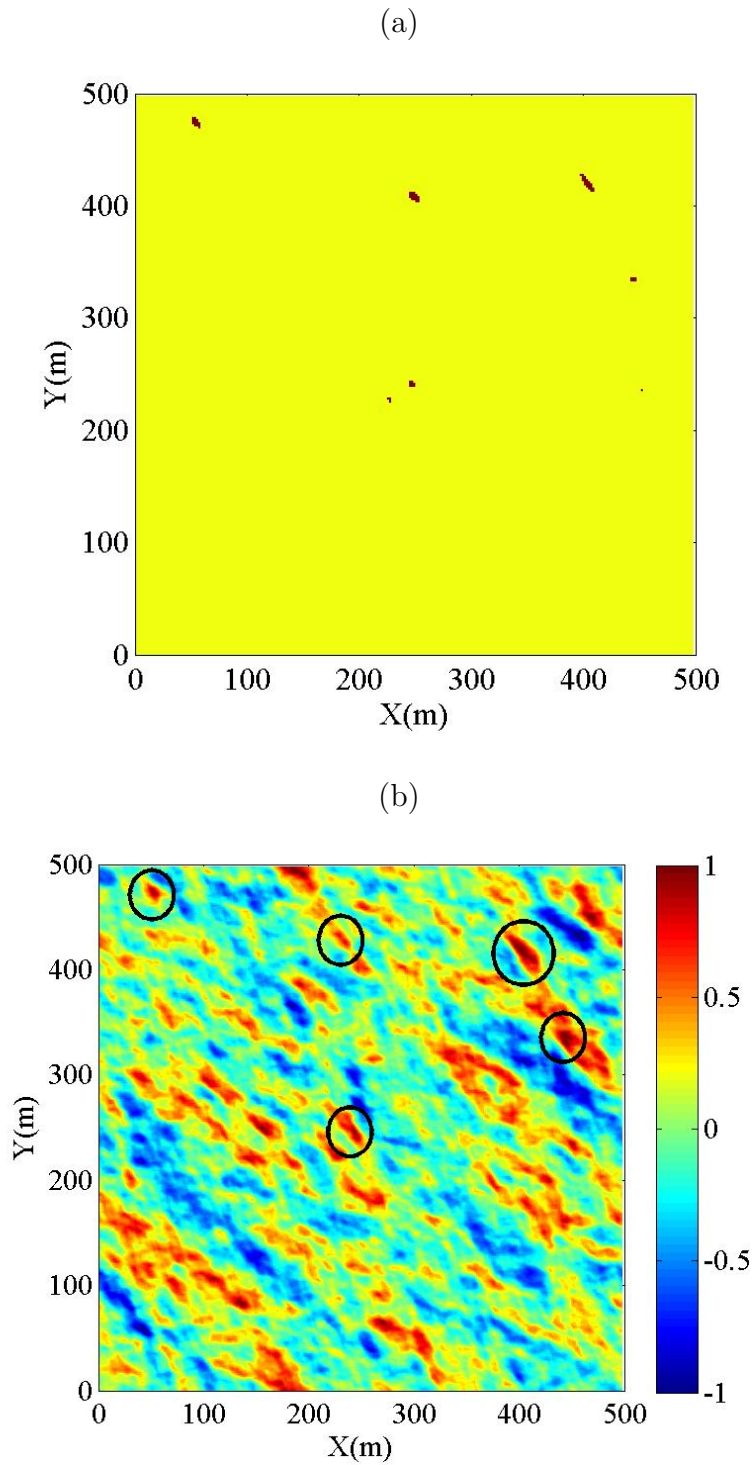


Figure 5.8: (a) Map of breaking regions at time 400 s. The red patches indicate regions where the vertical acceleration is less than the threshold of -0.4. (b) Predicted surface elevation at time 400 s. The black circles indicate locations where the model detected wave breaking.

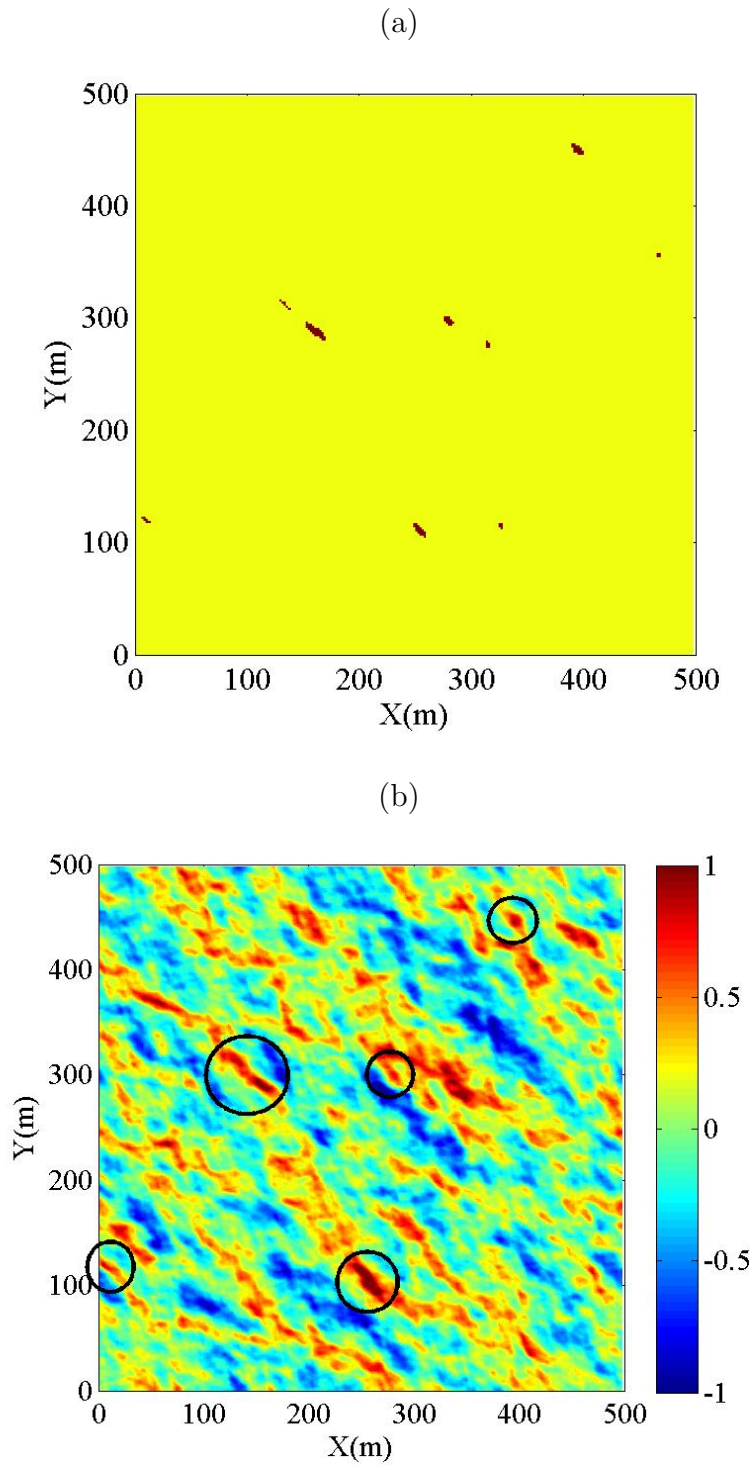
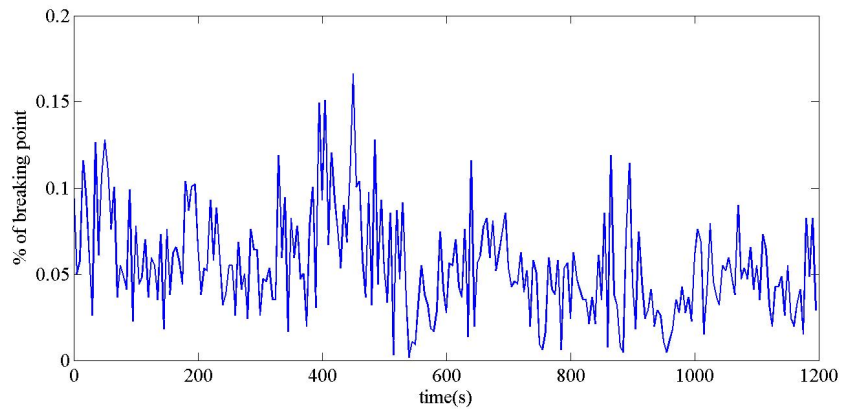
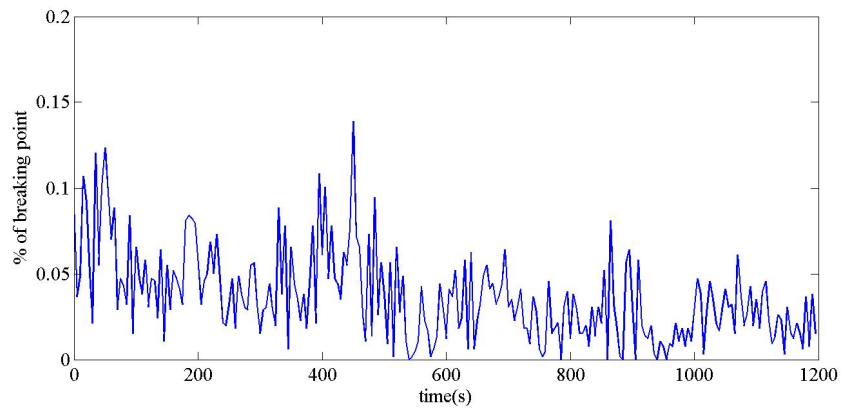


Figure 5.9: (a) Map of breaking regions at time 455 s. The red patches indicate regions where the vertical acceleration is less than the threshold of -0.4. (b) Predicted surface elevation at time 455 s. The black circles indicate locations where the model detected wave breaking.

(a) $\sigma=0.3$



(b) $\sigma=1.0$



(c) $\sigma=2.0$

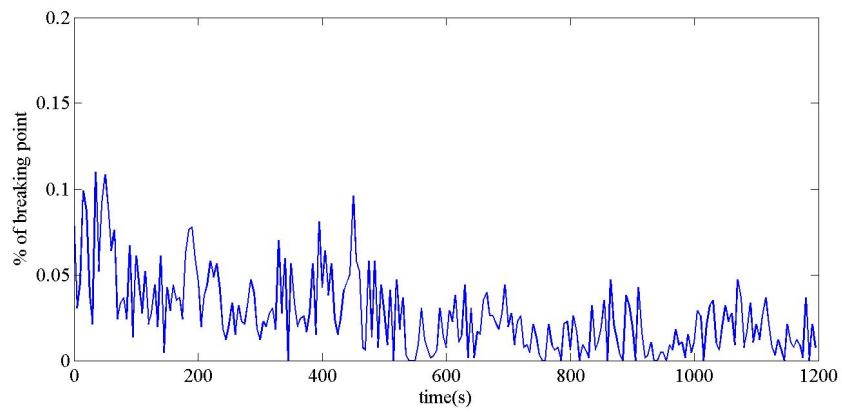


Figure 5.10: Percent of breaking point of cases with the strength of the damping constant (a) $\sigma = 0.3$, (b) $\sigma = 1.0$ and (c) $\sigma = 2.0$.

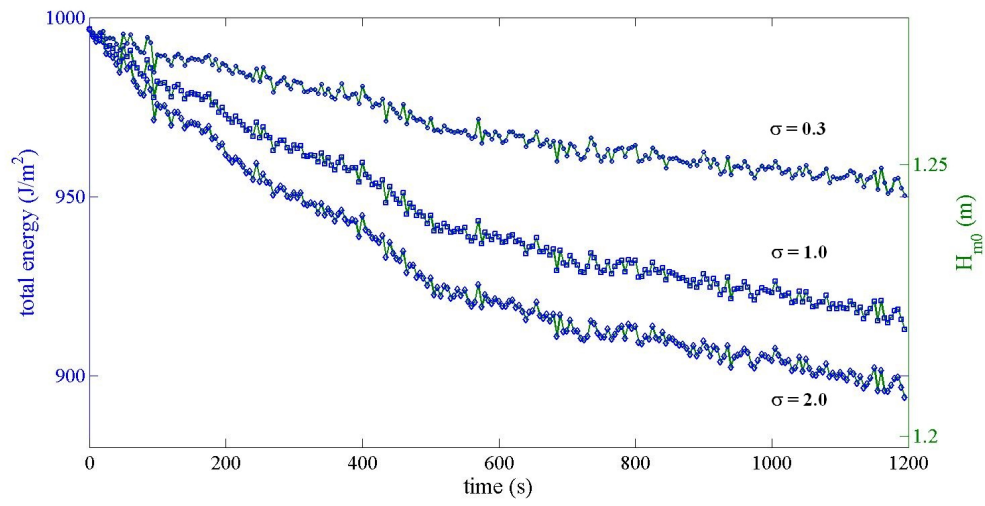


Figure 5.11: Energy density and significant wave height (H_{m0}) as a function of time for cases with the strength of the damping constant $\sigma=0.3$, 1.0 and 2.0.

Chapter 6

CONCLUSION

In this thesis, a three-dimensional nonlinear wave model has been parallelized using MPI for communication between processes and FFTW-MPI for computing Fourier transform. Wave breaking model and wave energy dissipation have been implemented into the model. The dynamics vertical acceleration criterion has been used to detect likely occurrence of wave breaking in a numerical domain. Adding pressure against the wave field is the technique used to absorb energy locally from waves that are about to break.

The parallelized model has been testing for both accuracy and performance. An idealized case of solitary wave and energy focusing nonbreaking wave group obtained from a laboratory experiment are used for examining an accuracy of the model while an initial Gaussian wave profile is used for checking performance. The results are satisfactory. The model has been applied to study energy focusing breaking wave groups from laboratory experiments and ocean random waves from field observation. It is found that the model predicts well the total energy dissipated in breaking events in laboratory experiments.

However, when using the large number of processors, speedup of the parallelized model decreases. Using hybrid method may help improve the speedup. The second level of parallelization could be either to parallelize the evolution of the Dirichlet-Neumann operator (DNO) as suggested by Nicholls (1998) or to use OpenMP to take advantage of SMP nodes as done in Larsgrd (2007). Also, improving de-aliasing part in the parallelized model will increase speedup. FFTs-alias-free version developed by Roberts (2012) may be used.

Further development of the model may involve an extensive testing of the model over a wide variety of wave conditions and breaking criteria. More realistic wave energy dissipation needs to be considered and implemented in the model. For simulations of ocean random waves, wind input during the simulation is another important factor which should be included in the model. These directions are envisioned for future work.

BIBLIOGRAPHY

- [1] Bayindir, C. 2009 “Implementation of a computational model for random directional seas and underwater acoustics.” *Master’s thesis*. University of Delaware.
- [2] Cao, Y., Beck, R.F. and Schultz, W.W. 1993 “An absorbing beach for numerical simulations of nonlinear waves in a wave tank.” *Proceedings, Eighth International Workshop on Water Waves and Floating Bodies*. Newfoundland, Canada.
- [3] Coifman, R. and Meyer, Y. 1985 “Nonlinear harmonic analysis and analytic dependence.” *Proc. Symp. Pure Math.* 43, 71-78.
- [4] Craig, W. and Sulem, C. 1993 “Numerical simulation of gravity waves.” *J. Comput. Phys.* 108, 73-83.
- [5] Dommermuth, D.G. and Yue, D.K.P. 1987 “A High-order spectral method for the study of nonlinear gravity waves” *J. Fluid Mech.* 184, 267-288.
- [6] Donelan, M.A., Hamilton, J. and Hui, W.H. 1985 “Directional spectra of wind-generated waves” *Phil.Trans. R. Soc. Lond.* A315, 509-562.
- [7] Frigo, M. and Johnson, S.G. 2003 “FFTW User’s Manual: version 2.1.5.” 16 March.
- [8] Larsgrd, N.M. 2007 “Parallelizing particle-in-cell codes with OpenMP and MPI.” *Masters thesis*. Norwegian University of Science and Technology.
- [9] Longuet-Higgins, M.S. 1963 “The generation of capillary waves by steep gravity waves.” *J. Fluid Mech.* 16, 138-159.
- [10] Longuet-Higgins, M.S. 1985 “Acceleration in steep gravity waves.” *J. Phys. Oceanogr.* 15,1570-1579.
- [11] Massel, S.R. 2007 “Ocean Waves Breaking and Marine Aerosol Fluxes.” Springer, New York.
- [12] Nicholls, D.P. 1998 “Traveling water waves: spectral continuation methods with parallel implementation.” *J. Comput. Phys.* 143, 224-240.
- [13] Ochi, M.K. and Tsai, C.H. 1983 “Prediction of occurrence of breaking waves in deep water.” *J. Phys. Oceanogr.* 13, 2008-2019.

- [14] Roberts, M. 2012 “Programming experience.” 21 March.
- [15] Schanz, U. 1997 “On the evolution of gravity-capillary waves in three dimensions.” *Dissertation*. University of Toronto.
- [16] Snyder, R.L. and Kennedy, R.M. 1983 “On the formation of whitecaps by a threshold mechanism. Part I: Basic formalism.” *J. Phys. Oceanogr.* 13, 1482-1492.
- [17] Snyder, R.L., Smith, L. and Kennedy, R.M. 1983 “On the formation of whitecaps by a threshold mechanism. Part III: Field experiment and comparison with theory.” *J. Phys. Oceanogr.* 13, 1505-1518.
- [18] Tanaka, M. 1986 “The stability of solitary waves.” *Phys. Fluids* 29, 650-655.
- [19] Tian, Z., Perlin, M. and Choi, W. 2012 “An eddy viscosity model for two-dimensional breaking waves and its validation with laboratory experiments.” *Phys. Fluids* 24, 036601.
- [20] Wu, C.H. and Nepf, H.M. 2002 “Breaking criteria and energy losses for three-dimensional wave breaking.” *J. Geophys. Res.* 107(C10), 3177, doi:10.1029/2001JC001077, 18p.
- [21] Xu, L. and Guyenne, P. 2009 “Numerical simulation of three-dimensional nonlinear water waves.” *J. Comput. Phys.* 228(22), 8446-8466.
- [22] Zakharov, V.E. 1968 “Stability of periodic waves of finite amplitude on the surface of a deep fluid.” *J. Appl. Mech. Tech. Phys.* 9, 190-194.